Petroleum Science (2018) 15:857–869
https://doi.org/10.1007/s12182-018-0264-8

ORIGINAL PAPER

Regeneration of Ag_XO@SBA-15 for reactive adsorptive desulfurization of fuel

Liqiong Wu[1] · Feiyan Ye[1] · Dong Lei[1] · Guang Miao[1] · Baoyu Liu[2] · Zhong Li[1] · Jing Xiao[1]

Received: 14 April 2018 / Published online: 10 October 2018

Abstract
Adsorbent regeneration is critical for a continuous adsorption–regeneration process and often underestimated. In this work, the regeneration of bifunctional Ag_XO@SBA-15 for [O]-induced reactive adsorptive desulfurization of liquid fuel is reported and further investigated. The spent Ag_XO@SBA-15 was regenerated in various types of solvents followed by calcination and tested in multiple desulfurization–regeneration cycles. The effects of regenerate solvents were also compared systematically. The original and regenerated Ag_XO@SBA-15 was characterized by X-ray diffraction, transmission electron microscopy, energy-dispersive X-ray spectroscopy, N_2 adsorption, X-ray photoelectron spectroscopy and atomic absorption spectrometry. The recovery of desulfurization capacity using various solvents follows the order of acetonitrile > acetone > ethanol > methanol > water. Owing to the complete reduction of silver species to Ag^0 and severe agglomeration of Ag^0, the bifunctional Ag_XO@SBA-15 demonstrating > 85% (2.60 mg-S/g) of sulfur removal dramatically reduced to < 46% (1.56 mg-S/g) after only 1st-cycle regeneration. It is suggested that polar organic species strongly adsorbed (or residual) on the spent Ag_XO@SBA-15, in that case, after solvent wash may contribute to the accelerated decomposition of Ag^+ to Ag^0 in the following calcination step. The desulfurization capacity decreased rather mildly in the later regeneration runs. Cautious choice of regeneration conditions and strategies to rational design stabilized adsorbents is required to avert the adsorbent deactivation.

Keywords Bifunctional · Regeneration · Oxidation · Adsorption · Deactivation

1 Introduction

Environment protection is an ongoing subject worldwide and becomes even urgent with more severe air pollution nowadays. Among various air pollutants, sulfur oxide (SO_x) is one typical hazard which has adverse effects on human health and the atmospheric environment (i.e., causing acid rain and generating fine particular matter) (Zhang et al. 2016b; Xia 2008; Mohammadian et al. 2017). It is estimated that half of the anthropogenic SO_2 arises for the emission from fossil-fuel combustion, including on-road vehicle sources and off-road mobile sources (Lu et al. 2010; Fan et al. 2009). In such circumstances, clean fuel research, especially ultra-deep desulfurization of transportation fuels, becomes a more and more important subject in environmental catalysis. The US Environmental Protection Agency (EPA) regulated a sulfur content of 30 ppmw in gasoline and 15 ppmw in diesel, and even lower sulfur content may be required in the future or for special use. Technically, refineries are facing great challenges to meet the fuel sulfur specification along with rather low operating costs and investment for ultra-deep desulfurization. Hydrodesulfurization (HDS) (Song 2003; Babich and Moulijn 2003; Song and Ma 2003) at high temperature ranging from 300 to 400 °C and high hydrogen pressure from 3 to 6 MPa converts organosulfur compounds to hydrogen sulfide (H_2S) over CoMo or NiMo

Edited by Xiu-Qin Zhu

Handling editor: Wen shuai Zhu

✉ Baoyu Liu
baoyu.liu@gdut.edu.cn

✉ Jing Xiao
cejingxiao@scut.edu.cn

[1] School of Chemistry and Chemical Engineering, South China University of Technology, Guangzhou 510640, China

[2] School of Chemical Engineering and Light Industry, Guangdong University of Technology, Guangzhou 510006, China

catalysts. Currently HDS is widely applied in refineries to remove sulfur from liquid hydrocarbon steams (Xiao et al. 2014). However, HDS achieves less efficiency in the removal of heterocyclic S-compounds such as benzothiophene (BT), dibenzothiophene (DBT) and their derivatives (González et al. 2016). Therefore, developing alternative non-hydrotreating approaches which could be used under ambient conditions and without high hydrogen consumption for effective ultra-deep desulfurization has attracted much interest (Miao et al. 2016; Sévignon et al. 2005).

Non-hydrotreating technologies, such as catalytic oxidative desulfurization (Piccinino et al. 2017; Wu et al. 2016; Li et al. 2016a, b), adsorption desulfurization (Lee and Valla 2017; Qin et al. 2016; Lei et al. 2016), biodesulfurization (Chaiprapat et al. 2015; Agarwal and Sharma 2010) and extraction desulfurization (Li et al. 2016a, b; Juliao et al. 2018; Bhutto et al. 2016) have been reported in the past decade. Among them, HDS coupled with selective adsorption of organic sulfur compounds has been considered as one potential technology (Song 2003) as HDS is efficient for desulfurization of high concentrations of organosulfur compounds, while adsorption can be advantageous for cleaning up the trace amount of stubborn organosulfur compounds which are very difficult to remove by HDS (Xiao et al. 2008, 2010). Reactive adsorptive desulfurization based on a reduced metal-based sorbent (namely S-Zorb) was developed by Phillips Petroleum and has been applied in industry (Gislason 2001). Besides, physical absorption showed advantages in easy desorption and recycling (Qiu et al. 2013; Hobson 1973), but hindered by less adsorption selectivity only targeting organosulfur compounds.

Previously, a selective catalytic adsorption desulfurization (CADS) approach coupling oxidation with adsorption for deep desulfurization was proposed (Guo et al. 2012; Li et al. 2015; Ma et al. 2007). In the CADS process, organosulfur compounds in fuels were oxidized to sulfoxides or sulfones, and then the oxidized sulfur compounds with higher polarity can be selectively adsorbed on the adsorbent surface to achieve ultra-deep desulfurization. The adsorbents served bifunctionally as an oxidation catalyst for thiophenes and as a selective adsorbent for sulfoxides/sulfones. Ren et al. (2016) investigated CADS of model diesel using TiO_2/SBA-15 under mild conditions, and high desulfurization capacity of 12.7 mg-S/g was achieved even at a low sulfur concentration of 15 ppmw-S. The CADS-TiO_2/SBA-15 mechanism involved the oxidation of DBT to $DBTO_2$ by cumene hydroperoxide and the simultaneous adsorption of $DBTO_2$ by TiO_2/SBA-15. Dou and Zeng (2014) developed a synthetic route to integrate thin mesoporous silica nanowires and achieved over 99% conversion of DBT to $DBTO_2$ in model diesel. The mesoporous silica served as catalyst and adsorbent to remove organosulfur compounds effectively. Previous work hinted that CADS via organic peroxides to convert thiophenic sulfur compounds to sulfones over adsorbent can be a plausible approach to enhance ADS selectivity for ultra-deep desulfurization. However, the high cost of organic peroxides may limit its application in industry, whereas further development of CADS processes via the abundant oxygen molecules in air can further push the way of the real applications of the CADS technology. In such case, how to activate the oxygen molecules in the air for the oxidation of thiophenes becomes critical. Xiao et al. (2013) demonstrated the desulfurization of commercial diesel by using TiO_2–CeO_2 mixed-oxide adsorbents with the addition of air to the fuel and found a strong promoting effect of air under ambient conditions, but the desulfurization capacity needs to be improved further. Silver nanoparticles (NPs) also possess the potential to activate oxygen molecules in the air (Le et al. 2012), while hexagonal mesoporous silica SBA-15 can serve as a promising platform for metal NPs because of its high surface area, large pore size and good stability (Dai et al. 2016; Verma et al. 2015). Beyond that, we recently demonstrated an [O]-induced reactive adsorptive desulfurization (RADS) approach using bifunctional Ag_X-O@SBA-15 adsorbent under ambient conditions. High desulfurization capacity and selectivity, as well as a high kinetic rate for deep desulfurization, were achieved (Ye et al. 2017). However, questions remain on how to regenerate the Ag_XO@SBA-15 adsorbent and how it behaves in multiple runs.

In this work, the regeneration of Ag_XO@SBA-15 for RADS of liquid fuel was explored and further investigated. The spent Ag_XO@SBA-15 adsorbent was regenerated by a solvent washing followed by calcination. The effect of various solvents was compared and further discussed in detail. The original and regenerated Ag_XO@SBA-15 samples were characterized by N_2 adsorption, powder X-ray diffraction (XRD), transmission electron microscope (TEM), energy-dispersive X-ray spectroscopy (EDS), X-ray photoelectron spectroscopy (XPS) and atomic absorption spectrometry (AAS). The deactivation mechanism of Ag_XO@SBA-15 during regeneration was closely investigated. The exploration of regeneration and deactivation mechanism disclosed in this work may provide guidance for cautious choice of regeneration conditions to avert the adsorbent/catalyst deactivation.

2 Experimental

2.1 Adsorbent syntheses

The supported Ag_XO@SBA-15 adsorbents were prepared by an incipient-wetness impregnation method assisted with ultrasound. For at least 12 h, 0.5 g SBA-15 (XFNANO Corp., China) was preheated in 110 °C. Then, 0.1545 g $AgNO_3$ was dissolved in 1.2 mL deionized water and added into SBA-15 drop by drop with ultrasonic mixing while stirring vigorously and with the ultrasound continuing for 30 min after the deposition. After that the sample was dried at 110 °C for 2 h and calcined at 400 °C for 4 h ramped at 1.5 °C/min. The as-prepared Ag_XO@SBA-15 adsorbents were stored in a desiccator before use.

2.2 Model fuels

The model fuels were prepared by dissolving 150 ppmw-S of benzothiophene (BT, 99%) in *n*-dodecane (AR, Guangdong Guanghua Chemicals Co., 99%).

2.3 Desulfurization experiments

The desulfurization experiments were carried out in a batch reactor under ambient conditions, with 10 cc/min air flowing continuously for 4 h, and the fuel-to-sorbent ratio (w/w) was 20. And then the sulfur concentrations in initial and desulfurized fuels were analyzed by a high-performance liquid chromatogram (HPLC) equipped with a UV-Vis detector at 290 nm for BT and an ODS-C18 column at the flow rate of 1.0 $cm^3\ min^{-1}$. In addition, the adsorption of BT over Ag_XO@SBA-15 without air flow was tested for comparison.

2.4 Regeneration of Ag_XO@SBA-15

In the regeneration process, the spent adsorbent was washed with an excess amount of acetonitrile or other solvents, including deionized water, methanol, ethanol and acetone assisted with ultrasound for 10 min and then filtered. The solid was dried in 110 °C for 30 min, and a part of the sample was stored in a desiccator before being tested in the next desulfurization cycle when another part was calcined at 400 °C for 4 h ramped at 1.5 °C/min before being stored. 15% Ag_XO@SBA-15 samples which were tested under the RADS system for four consecutive regeneration cycles were denoted as orig. 0, recy. 1, recy. 2, recy. 3 and recy. 4, respectively.

2.5 Characterization of Ag_XO@SBA-15

Powder X-ray diffraction (XRD). XRD data were obtained by a Bruker D8 Advance X-ray diffractometer with Cu Kα radiation at room temperature with a scan speed of 2 °C/min and a step length of 0.02° at the range of 5°– 60° (2θ).

Transmission electron microscopy (TEM) and energy-dispersive X-ray spectroscopy (EDS). The morphology and element mapping of the Ag_XO@SBA-15 samples were performed on a JEM-2100F field emission electron microscope operating at 180 kV with supplied software for automated electron tomography.

N_2 adsorption. N_2 adsorption/desorption isotherms were obtained at − 160 °C on a Micromeritics' Accelerated Surface Area and Porosimetry Analyzer 2020 (ASAP 2020) equipped with commercial software for calculation and analysis. The pore textural properties such as specific Langmuir surface area and Brunauer–Emmett–Teller (BET) surface area were obtained by analyzing the N_2 adsorption isotherms. The pressure ranges used for the BET surface area calculations were $0.05 < P/P_0 < 0.25$. (Based on the three consistency criteria pore volume data and pore size distribution calculation also were provided by the ASAP 2020 equipped with the software based on density functional theory (DFT).) The samples were outgassed at 186 °C for 8 h before each measurement.

Atomic absorption spectrometry (AAS). Ag loading was measured by Z-2000 AAS with 1800 line/mm diffraction raster and 200 nm wave length, 190–900 wave range. Its focal distance is 400 mm, the bottom line of the dispersion rate is 1.3 nm/mm, and spectral bandwidth has four files of 0.2, 0.4, 1.3 and 2.6. The average current value is around 2.5–20 mA.

X-ray photoelectron spectroscopy (XPS) was examined by a Kratos Axis Ultra DLD XPS spectrometer. The spectrum of each sample was recorded by monochromatized Al Kα radiation using the binding energy (284.6 eV) of amorphous C1s as the reference.

3 Results and discussion

3.1 Adsorbent regeneration

In our previous work, the bifunctional Ag_XO@SBA-15 adsorbent for [O]-induced reactive adsorption desulfurization (RADS) was reported, and the desulfurization capacity reached 2.62 mg-S/g with the addition of air under ambient conditions (Ye et al. 2017). The RADS mechanism of Ag_XO@SBA-15 illustrated that the thiophenic compounds can be oxidized to sulfones by oxidative nanosize [O]-retaining AgO on SBA-15 (the AgO transforms to Ag_2O

after desulfurization) in the absence of air or by the resulting or existing catalytic nanosize Ag_2O and Ag (in small amounts) in the presence of air. The transformed sulfones adsorbed on the adsorbent through a stronger R_2SO_2-Ads H-bonding interaction through the oxygen atom in sulfones with the silanol groups on the surface of the silica support, rather than R_2S-Ads interaction (Xiao et al. 2015), resulting in a dramatically enhanced ADS capacity. In this work, the adsorbent regeneration of Ag_X-O@SBA-15 is further investigated for a continuous adsorption–regeneration process.

Different solvents were applied to wash the spent Ag_X-O@SBA-15 without further calcination. Effect of solvents on RADS capacity of the spent Ag_XO@SBA-15 is shown in Fig. 1. By washing the spent Ag_XO@SBA-15 with different solvents of water, acetonitrile, methanol, ethanol and acetone, its RADS capacity recovered to 0.75, 1.12, 1.00, 1.02 and 1.10 mg-S/g, respectively. The recovery of desulfurization capacity using various solvents followed the order of acetonitrile > acetone > ethanol > methanol > water, inconsistent with the polarity of the solvents, which decreased in the order of water > acetonitrile > methanol > ethanol > acetone (Li et al. 2009). Acetonitrile showed the highest recovery, probably due to the "like dissolves like" principle as sulfone can be easily dissolved in acetonitrile, and the low surface tension enhances mass transfer (Lu et al. 2016). In the case of water, it is hard to dissolve the residual organic species from the spent Ag_XO@SBA-15, as sulfone cannot be dissolved in water, forming an immiscible mixture (Li et al. 2009). The pictures of the regenerated Ag_XO@SBA-15 after solvent wash are shown in the inset of Fig. 1. As confirmed, the acetonitrile washing showed the most similar color to the fresh material and also demonstrated the maximum recovery of desulfurization capacity. Therefore, acetonitrile was chosen as the washing solvent in the later studies.

Intended to further remove adsorbed species, i.e., sulfoxides/sulfones, thiophenic compounds, fuel compositions, residue of the polar solvent of acetonitrile on the spent Ag_XO@SBA-15, the adsorbent was regenerated by an acetonitrile wash followed with oxidative air treatment (Ren et al. 2016; Miao et al. 2015). Figure 2 shows the desulfurization uptakes of the 15% Ag_XO@SBA-15 in 4 consecutive RADS-regeneration cycles. The regenerated Ag_XO@SBA-15 shows the desulfurization uptakes of 2.60 (original), 1.56, 1.19, 1.06, 1.05 mg-S/g in the first four cycles, suggesting partial recovery of RADS capacity. The uptake of Ag_XO@SBA-15 after calcination followed by solvent washing (1.56 mg-S/g) is higher than that after solvent washing only (1.12 mg-S/g), suggesting oxidative air treatment is effective to further recover desulfurization sites on the spent Ag_XO@SBA-15 to some extent. It is noticeable that after the 1st-cycle regeneration, the desulfurization capacity of Ag_XO@SBA-15 decreased nearly 40%, yet the desulfurization capacities of Ag_XO@SBA-15 after the later consecutive regeneration runs decreased slightly. The results suggested that the active sites (either catalytic or adsorptive sites) on the Ag_XO@SBA-15 for BT catalytic oxidation adsorption cannot be fully regenerated, and the deactivation mechanism in different regeneration runs may vary. The deactivation mechanism in varied regeneration runs is worthy of further exploration.

Knowing the desulfurization capacity in the RADS process integrates adsorption capacity of BT and [O]-

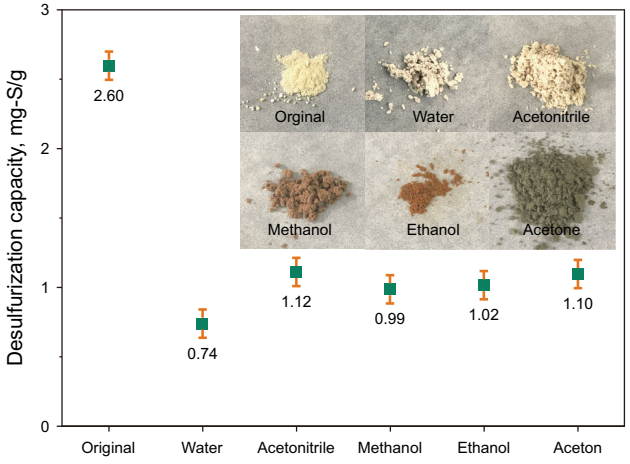

Fig. 1 Desulfurization capacity of the spent Ag_XO@SBA-15 by various types of solvent wash. Inset. Pictures of Ag_XO@SBA-15 after solvent wash. (RADS conditions: fuel-to-sorbent ratio of 20:1 (w/w), fuel of 150 ppmw-S BT in *n*-dodecane, air bubbled in at ambient conditions)

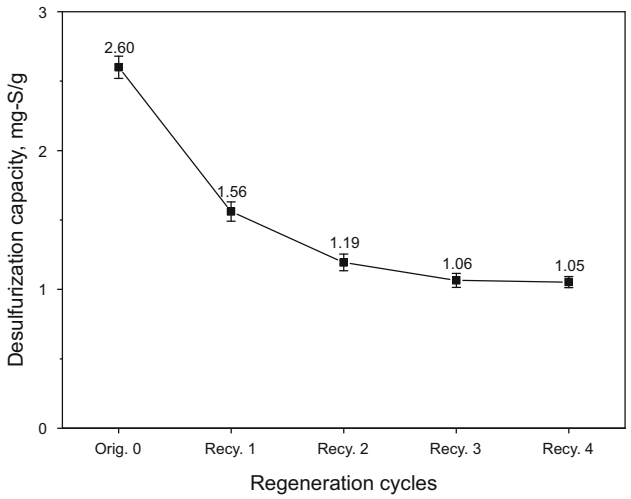

Fig. 2 BT desulfurization capacities of the 15% Ag_XO@SBA-15 adsorbent at 4 consecutive RADS-regeneration cycles. (RADS conditions: fuel-to-sorbent ratio of 20:1 (w/w), fuel of 150 ppmw-S BT in *n*-dodecane, air bubbled in at ambient conditions)

induced desulfurization capacity of chemically transformed sulfones (BTO_2), the contributions from both parts may vary with regeneration runs. To understand the decrease in sulfur uptakes in both parts during regeneration, desulfurization under air ([O]-induced adsorptive desulfurization) and nitrogen (sole adsorptive desulfurization) was compared. Figure 3 shows the desulfurization capacity of the regenerated Ag_XO@SBA-15 in the 1st cycle and 4th cycle compared to the original fresh one. The original Ag_X-O@SBA-15 showed a much lower desulfurization capacity of 1.71 mg-S/g under nitrogen (sole adsorption) than that under air ([O]-induced RADS of 2.60 mg-S/g), and the difference illustrates the contribution from the [O]-induced desulfurization. After 1st cycle of regeneration, the desulfurization capacity of Ag_XO@SBA-15 under air and nitrogen decreased to a similar value of $\sim$ 1.6 mg-S/g. The results suggested the complete loss of [O]-induced desulfurization capacity only after 1-run regeneration, referred to ΔQ_1 in Fig. 3. The inference was further supported by the GC–MS results, as only BT was detected on the spent Ag_XO@SBA-15 under air, and no sulfone was detected either in the eluent (acetonitrile solvent after washing the spent sorbent) or in the treated fuel. It should be mentioned that after losing the [O]-induced desulfurization capacity in the 1st run, the adsorption capacity decreased much more mildly (referred to ΔQ_2 in Fig. 3) even after multiple regeneration runs. The loss of [O]-induced desulfurization capacity may relate to the irreversible loss of the oxidation or catalytic oxidation sites on SBA-15, i.e., nanosize AgO, AgO_2 and Ag particles, while the loss of adsorption capacity of BT may be caused by the damaged or reduced amount of adsorption sites, which will be further characterized in the next session.

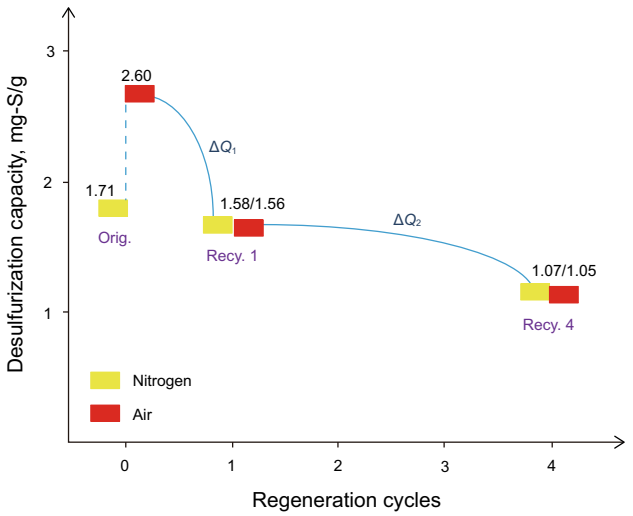

Fig. 3 Desulfurization capacity over Ag_XO@SBA-15 original and recycled samples under air and nitrogen. (ΔQ_1: complete loss of [O]-induced desulfurization capacity after 1-run regeneration. ΔQ_2: mild decrease in adsorption capacity. Reaction conditions: fuel-to-sorbent ratio of 20:1 (w/w), fuel of 150 ppmw-S BT in *n*-dodecane, air and nitrogen bubbled in at ambient condition)

3.2 Sorbent characterizations

Figure 4a, b shows the wide and low-angle XRD patterns of Ag_XO@SBA-15 samples at four consecutive RADS-regeneration cycles. No intense diffraction peaks of silver species were detected on the fresh Ag_XO@SBA-15, indicating high dispersion of silver nanoparticles. The particle size of Ag_XO is calculated to be 3–4 nm (by TEM in Fig. 5), below the detection limit of the XRD instrument, as reported in the literature (Zhang et al. 2016a; Perkas et al. 2013). In sharp contrast, two diffraction peaks at 38.1° and 44.1° appeared in all of the regenerated samples, corresponding to the reflections of (111) and (200) crystalline planes of face-centered cubic (*fcc*) structure of metallic Ag^0 (JCPDS Card No. 04-0783) (Gu et al. 2011). The results indicated that the multivalent silver nanoparticles reduced to zero-valence Ag^0 after oxidative air treatment. Moreover, the XRD results suggested that the particle size of silver increased after regeneration. It should be noticed that the diffraction intensity of both peaks increased with increasing runs of regeneration. The Scherrer equation (Borchert et al. 2005; Ocakoglu et al. 2015) $D = 0.89\lambda/\beta\cos\theta$ was used to calculate the crystalline size (D) of the recycled Ag_XO@SBA-15, where λ, β and θ were X-ray wavelength, FWHM of diffraction peak and Bragg's diffraction angle, respectively. Instrumental broadening was taken into account in the calculation, and the result is listed in Table 1. Based on the FWHM of Ag(111) diffraction peaks at 0.295°, 0.284°, 0.280° and 0.269°, the crystalline sizes of the Ag particles in 1–4 runs became 27.2, 28.5, 28.7 and 30.1 nm, respectively. The data indicated that the silver particles sharply aggregated from the average particle size of $\sim$ 3 to $\sim$ 27 nm after 1st-cycle regeneration, and further increased slightly after the latter runs of regeneration.

From the low-angle XRD patterns, the three peaks at 2θ of 0.92°, 1.60° and 1.84° were corresponding to (100), (110), (200) planes of the hexagonal mesostructure (Dai et al. 2016), respectively. The results suggested that the hexagonal order was well maintained, but slight loss of peak intensity for the low-angle reflections was observed after multiple runs of regeneration. It was noticed that the diffraction peaks of the initial Ag_XO@SBA-15 samples shifted to higher angle in the recycled Ag_XO@SBA-15 samples, indicating the decrease in SBA-15 lattice parameters after oxidative air treatment. Table 1 lists the interplanar spacings d_{100} and the unit cell parameter a_0 of Ag_XO@SBA-15 in multiple runs of regeneration. Slight decrease in d_{100} (from 9.6 to 9.3 nm after 4 runs) and a_0

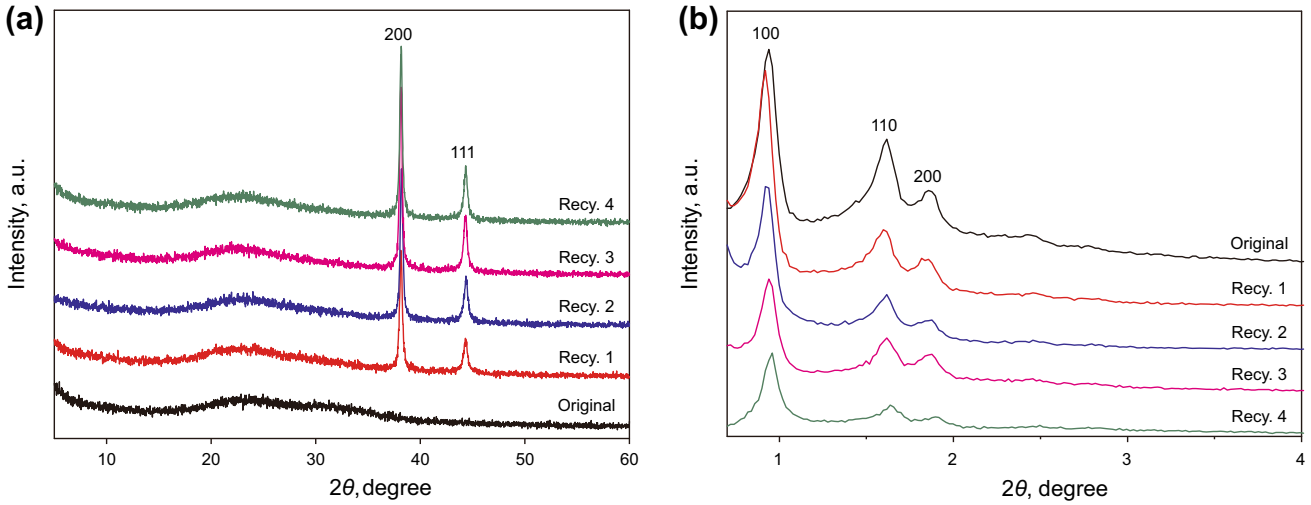

Fig. 4 **a** Wide and **b** low-angle XRD patterns of Ag_XO@SBA-15 at four consecutive RADS-regeneration cycles

(from 11.1 to 10.7 after 4 runs) can be found, and it further suggested that the mesoporous structure of Ag_XO@SBA-15 nanocomposites showed unit cell shrinkage (Ebin et al. 2010; Aronson et al. 1997) with the increase in regeneration cycles. It is believed that the oxidative air treatment introduced defects that can lead to slight contraction of the framework. This framework contraction may result from further silver condensation during regeneration.

To complement the XRD analysis, transmission electron microscope (TEM) and energy-dispersive X-Ray spectroscopy (EDS) were employed to directly observe the change on Ag crystalline particles of Ag_XO@SBA-15. Figure 5a-1, a-2 shows the TEM image of the fresh Ag_XO@SBA-15. Multivalent silver nanoparticles were detected and dispersed homogeneously in the channel of SBA-15 supports. The spherical nanoparticles possess d-spacing of 0.241, 0.216, 0.233 and 0.205 nm, corresponding to the (111) and (213) planes of AgO, (101) plane of Ag_2O and (200) plane of Ag, respectively. The corresponding EDS elemental mapping (Fig. 5a-3) shows that the Ag species is well dispersed in the fresh sample. The particle-size histogram (Fig. 5a-4) reveals that the particle size of Ag nanoparticles displays a normal distribution, and their average size is 1.65 ± 1.17 nm. In contrast, the images of Ag_XO@SBA-15 after 1st-cycle regeneration (Fig. 5b-1, b-2) reveal that the Ag nanoparticles agglomerated to quite large spherical particles. The particles possess *d*-spacing of 0.205 and 0.232 nm, corresponding to the (200) and (111) planes of Ag^0, respectively, with the particle size of silver species as large as 50.6 ± 8.7 nm. The particle size detected by TEM is much larger than the calculated value from XRD, because the particle size calculated by Scherrer equation is the average size of silver particles and the silver particles on the surface of Ag_XO@SBA-15 detected by TEM are partially agglomerated, as reported in the literature (Ebin et al. 2010). Besides, the corresponding EDS elemental mapping (Fig. 5b-3) reveals that the silver particles on Ag_XO@SBA-15 are partly aggregated after regeneration. And silver clusters further aggregated to larger silver particles of 52.3 ± 13.5 nm after four continuous regeneration cycles (Fig. 5c-1, c-2). Corresponding EDS (Fig. 5c-3) showed the silver particles aggregated more intuitively.

From the result of XRD and TEM/EDS, a conjecture is that the desulfurization capacity decreased sharply after the 1st-cycle regeneration because the active high-valence AgO and Ag_2O were reduced to zero-valence Ag^0 and the metallic silver nanoparticles aggregated to bigger ones which resulted in the complete loss of [O]-induced desulfurization capacity of Ag_XO@SBA-15. The presence of Ag^0 in regenerated samples was further confirmed in XPS (Fig. 6), though Ag^0 was also detected in the fresh sample via XPS, which was attributed to the fact that nanosize silver species in Ag_XO@SBA-15 are readily reduced to the elemental Ag^0 at high vacuum (10^{-7} Pa for 6 h pretreatment in XPS, as stated in our previous work) (Ye et al. 2017). In the latter regeneration runs, the desulfurization capacity decreased slightly, because the mild aggregation of Ag^0 particles resulted in a gentle decrease in adsorption capacity of BT.

From our previous work, the optimized adsorption configurations of the possible functionalities of Ag^0, Ag_2O and surface silanol group Si–OH were calculated (Le et al. 2012). The fresh Ag_XO@SBA-15 and, in the presence of air, BT were transferred to BTO_2 by oxidative AgO or oxygen catalyzed by Ag_2O. In this case, BTO_2 has a shorter bond with Si–OH (2.01 Å) than Ag (2.72 Å) or Ag_2O (2.75 Å), suggesting BTO_2 preferentially adsorbs on Si–OH, which explains the enhanced desulfurization capacity after RADS. On the other hand, the bond distance for BT

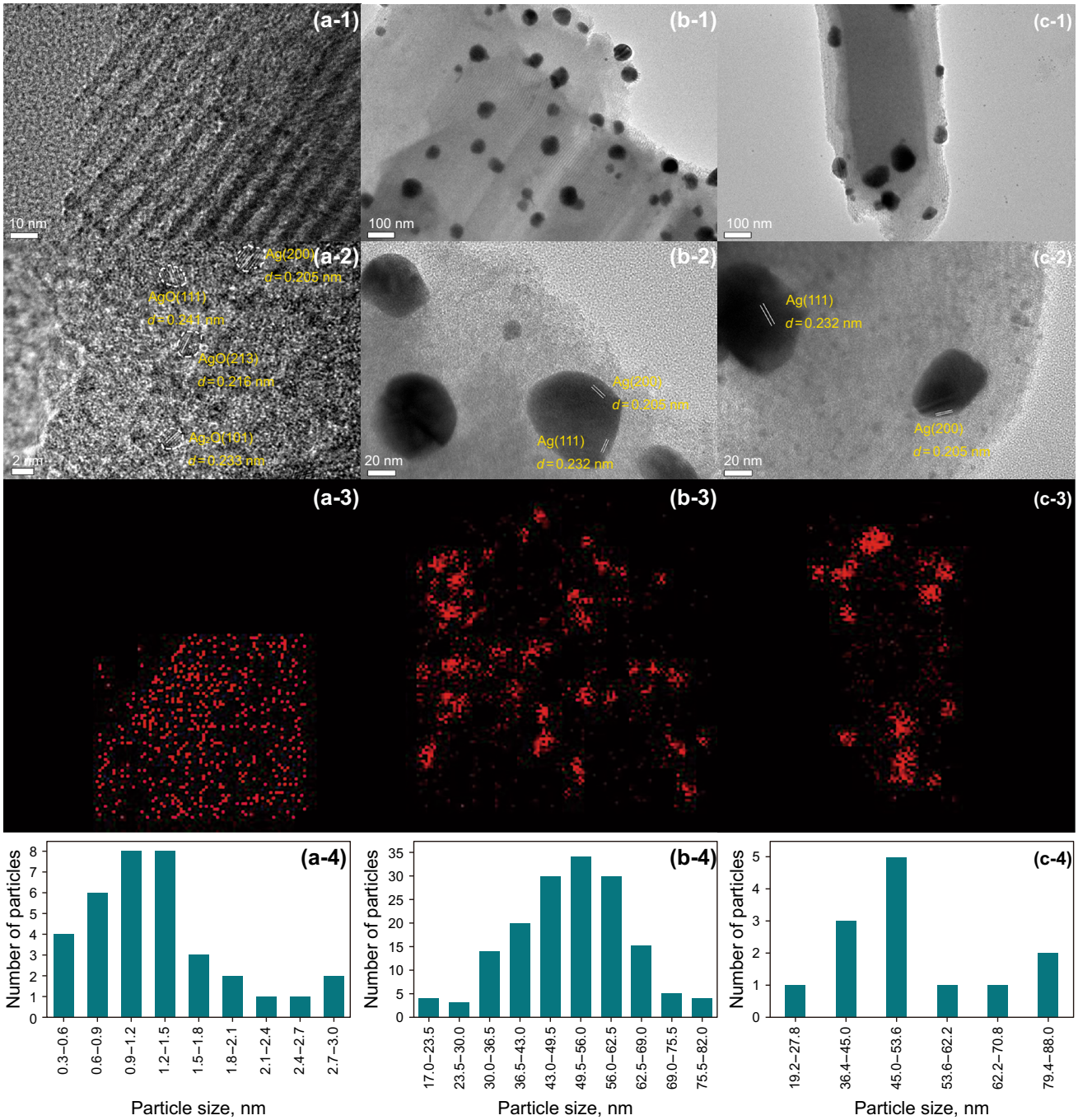

Fig. 5 TEM, EDS and particle-size histogram of three distinctive stages in four consecutive RADS-regeneration cycles of Ag_XO@SBA-15: series **a**–**c** for sample orig. 0, recy. 1, and recy. 4

follows the order of Ag_2O (2.39 Å) < Ag (2.65 Å) < Si–OH (3.43 Å), suggesting BT adsorbs on silver sites preferentially. Hence, in the RADS system, the affinity between the adsorbents and adsorbates follows the order of BTO_2–(Si–OH) > BT–Ag_2O > BT–Ag > BTO_2–Ag > BTO_2–Ag_2O > BT–(Si–OH). The strong affinity of BTO_2–(Si–OH) resulted in the high desulfurization capacity of the fresh Ag_XO@SBA-15. However, after the regeneration of Ag_XO@SBA-15, the major silver species presented on SBA-15 is non-oxidative and bulky Ag^0. On the one hand, the dominant adsorbent–adsorbate affinity transferred from strong BTO_2–(Si–OH) through [O]-induced desulfurization to relative weak BT–Ag^0 interaction through pi-complexation. On the other hand, from the result of XRD (Fig. 4) and TEM (Fig. 5), the severe agglomeration of silver species is detected, that is to say,

Table 1 Textural properties of 15% Ag_XO@SBA-15 at 4 consecutive RADS-regeneration cycles

Entry	d_{100}	a_0	S_{BET}	V_{BJH}	D^a_{BJH}	w^b
1	9.61	11.12	489.24	0.72	5.53	5.57
2	9.54	11.04	473.71	0.72	5.58	5.42
3	9.52	11.02	447.03	0.69	5.60	5.40
4	9.50	11.00	428.90	0.68	5.66	5.34
5	9.32	10.72	413.22	0.66	5.99	4.71

S_{BET}, specific surface area (m^2/g); V_{BJH}, pore volume (cm^3/g); D_{BJH}, pore diameter (nm); a_0, cell parameters (nm); d_{100}, interplanar spacing (nm); w, wall thickness (nm)

[a]Calculated from the desorption branch

[b]$w = a_0 - D_{BJH}(a_0 = 2d_{100}/\sqrt{3})$

the amount of exposed adsorption sites of Ag^0 on SBA-15 for BT also decreased, resulting in dramatically decreased desulfurization capacity after regeneration.

Figure 7a, b shows the nitrogen adsorption–desorption isotherms and the corresponding pore width distribution of Ag_XO@SBA-15 at four consecutive RADS-regeneration cycles referred to the SBA-15 substrate, with the textural properties as listed in Table 1. According to the IUPAC classification (Malakooti et al. 2013), the nitrogen adsorption–desorption isotherms of SBA-15 and Ag_X-O@SBA-15 original and recycled samples belong to typical IV isotherms, suggesting that all the support SBA-15 and Ag_XO@SBA-15 samples after regeneration retain mesoporosity with two-dimensional hexagonal structures (George et al. 2005). However, Type H_1 loops are observed on the Ag_XO@SBA-15, while an H_2 hysteresis loop is observed in SBA-15 (Kruk and Jaroniec 2001). In fact, an H_1 hysteresis loop was often reported for the materials that consisted of agglomerates or compacts of approximately spherical particles arranged in a fairly uniform way (Sing et al. 1985), and H_2 hysteresis loops were observed for materials with relatively uniform channel-like pores (Kruk and Jaroniec 1997), which correspond to the silver impregnation and agglomeration after regeneration of Ag_XO@SBA-15 and mesoporous channels of SBA-15, respectively. Meanwhile, the adsorbed N_2 amounts decreased after loading Ag_XO on SBA-15, but only a gentle decline was observed in Ag_XO@SBA-15 in four consecutive regenerations, suggesting that the porosity of Ag_XO@SBA-15 remained almost the same with only a slight decline.

As shown in Table 1, S_{BET} of SBA-15 and Ag_X-O@SBA-15 in multiple runs is 723.6, 489.2, 473.7, 447.0, 428.9 and 413.2 m^2/g, respectively. BET surface area decreased sharply after silver impregnation and only slightly after regenerations. A similar trend was observed in the decrease in pore volumes of SBA-15 and Ag_X-O@SBA-15 in multiple runs, corresponding to 1.15, 0.72, 0.72, 0.69, 0.68 and 0.66 cm^2/g, respectively. Considering that both the S_{BET} and the sulfur adsorption capacity decrease gradually, a linear fitting between S_{BET} and sulfur adsorption capacity is presented in Fig. 8. Except the fresh Ag_XO@SBA-15, sulfur adsorption capacity (Q) decreases with S_{BET} of Ag_XO@SBA-15 in latter runs of regeneration, which can be fitted to $Q = 0.0087 \times S_{BET} - 2.62$ with correlation coefficients (R^2) of 0.84. The decreased S_{BET} in multiple runs can be associated with the agglomeration of silver particles, while retaining similar pore sizes (Fig. 7b).

Metal leaching is another concern for multirun regeneration, which was studied with AAS (Butler et al. 2015). Silver content of Ag_XO@SBA-15 in multiple runs was measured as 15.0%, 15.2%, 15.4%, 15.5% and 15.6%, respectively (Fig. 9), suggesting no leaching of silver species after cycles of regeneration. It can be noted that the silver amount even increased slightly after cycles of regenerations. One conceivable explanation is the

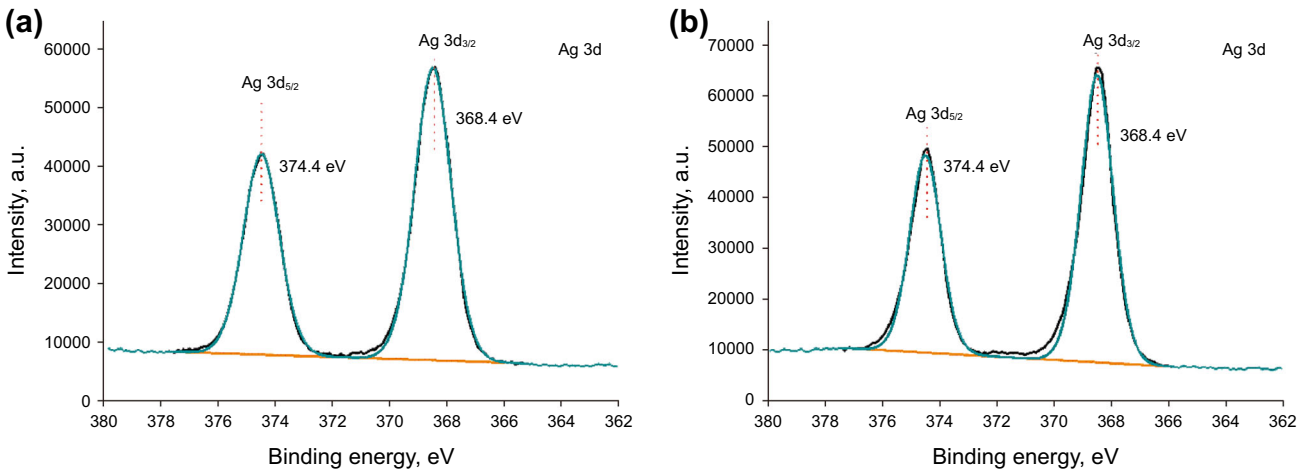

Fig. 6 The XPS spectra of Ag 3*d* from the fractured surfaces of the **a** Ag_XO@SBA-15 original sample and **b** Ag_XO@SBA-15 recycled sample

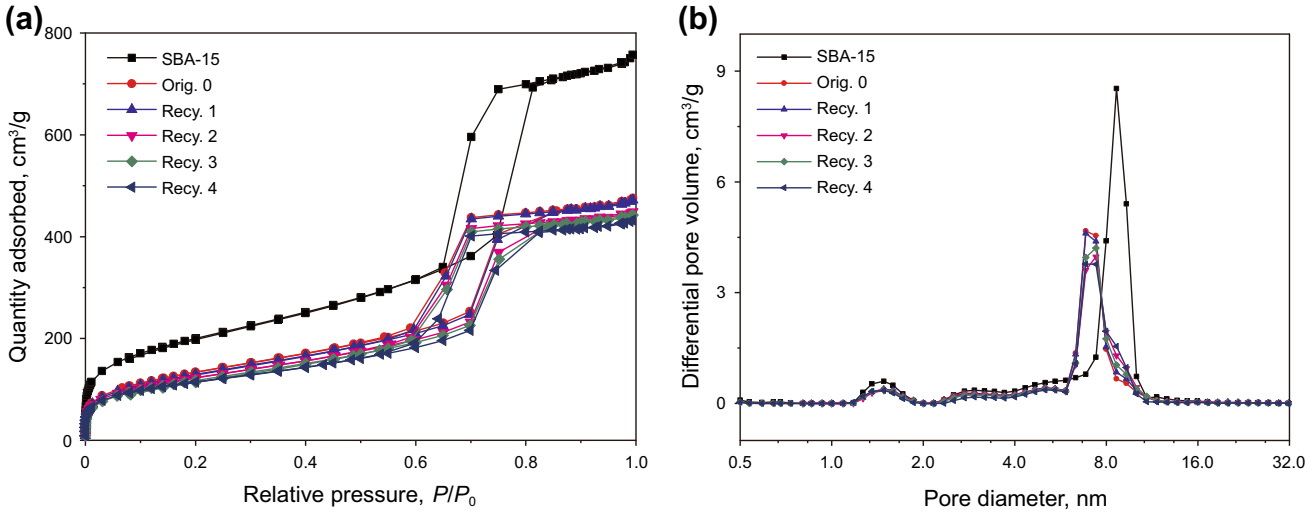

Fig. 7 Nitrogen adsorption–desorption isotherms and the corresponding pore width distribution of 15% Ag_XO@SBA-15 at five consecutive RADS-regeneration cycles

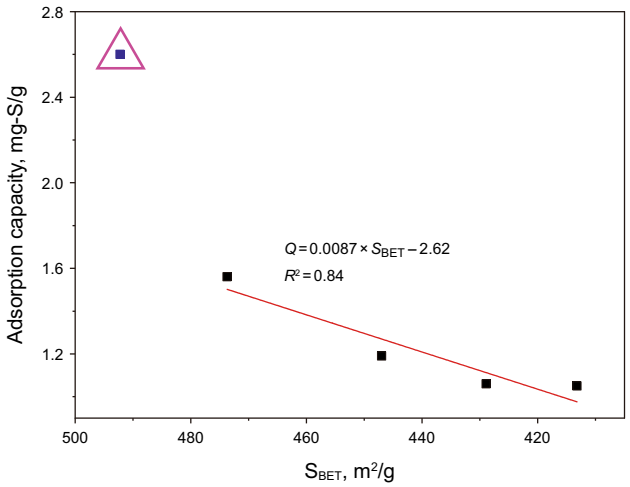

Fig. 8 Correlation of sulfur adsorption capacity and S_{BET}

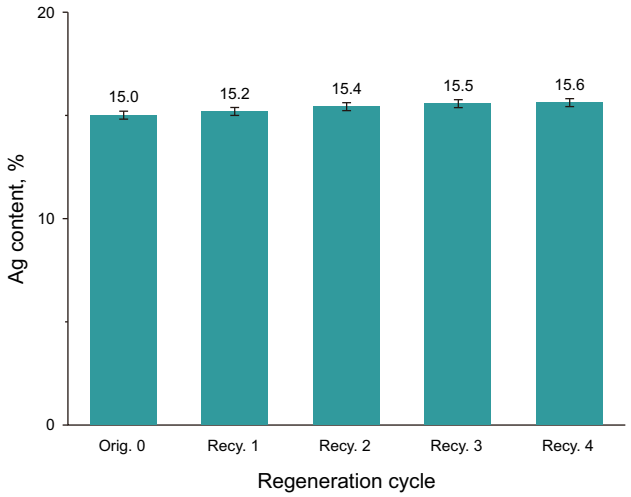

Fig. 9 The Ag content of Ag_XO@SBA-15 at four consecutive RADS-regeneration cycles detected by AAS

reduction of AgO/Ag_2O on the fresh sample to metallic Ag^0 of Ag_XO@SBA-15, resulting in the loss of oxygen atoms, and the decrease in the background denominator, so the overall content of Ag element increased. Theoretically, the complete reduction of AgO and Ag_2O to Ag would result in the increase in Ag content to 15.7% and 15.3%, respectively (Zvereva and Trunova 2012).

From the above analysis, the deactivation mechanism of Ag_XO@SBA-15 after regeneration can be deduced. After the 1st-cycle regeneration, high-valence AgO/Ag_2O reduced to zero-valence Ag^0 after oxidative air treatment, and much larger aggregated Ag^0 particles, resulting in the complete loss of oxidation capacity of Ag_XO@SBA-15, and the affinity between the adsorbates and adsorbents decreased. Meanwhile, the adsorption affinities as well as the amount of adsorption sites decreased after 1st cycle of regeneration, resulting in sharply decreased desulfurization capacity. In the latter regeneration cycles, the further aggregation of Ag^0 particles and the mild decrease in S_{BET} of Ag_XO@SBA-15 resulted in the gradual slight decrease in the desulfurization capacity in the latter regenerations. Nevertheless, the specific factors leading to the reduction or agglomeration is worthy to be further explored.

3.3 Effect of regeneration steps

Considering the severe deactivation of Ag_XO@SBA-15 in the first regeneration, further work was carried out to ascertain which step or steps in regeneration made the deactivation occur. Figure 10a shows the desulfurization capacity of Ag_XO@SBA-15 samples with different

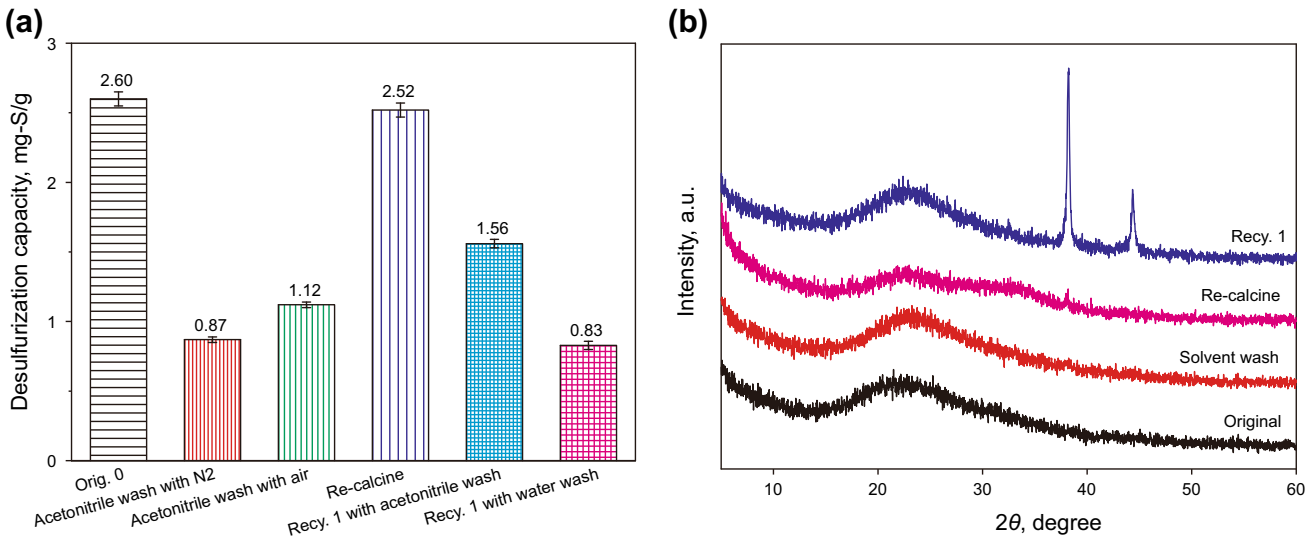

Fig. 10 **a** Desulfurization capacity of Ag_XO@SBA-15 after different treatments and **b** the corresponding XRD patterns (reaction conditions: fuel-to-sorbent ratio: 20:1 (w/w), fuel: 150 ppmw-S BT in *n*-dodecane, air bubbled in at ambient pressure)

regeneration treatments, and corresponding XRD patterns of the resulting samples are shown in Fig. 10b. The regenerated sample was tested in desulfurization under air and nitrogen, and their sulfur capacities are 1.12 mg-S/g and 0.87 mg-S/g, respectively. The one under air exhibited higher desulfurization capacity than that under nitrogen, suggesting portion of catalytic sites for sulfur oxidation recovered after the acetonitrile solvent washing. The corresponding XRD patterns (sample solvent wash) show that no Ag diffraction peak was detected, indicating that individual operation of a solvent washing would not lead to the agglomeration of silver particles. However, the solvent itself is likely to remain and block the active sites on the adsorbent surface, resulting in reduced desulfurization capacity. Hence, the step of followed-up calcination is necessary to remove the residual species in common regeneration. However, the desulfurization capacity recovered only 46% after calcination (1.56 mg-S/g), indicating that Ag_XO@SBA-15 deactivated during calcination. To rule out the possibility of the deactivation of Ag_XO@SBA-15 in longer calcination time, the re-calcination of the fresh Ag_XO@SBA-15 sample without desulfurization test (sample re-calcine) was conducted and the desulfurization capacity reached up to 2.52 mg-S/g, 97% of the desulfurization capacity of the Ag_XO@SBA-15 fresh sample, suggesting that the loss of desulfurization capacity may not relevant with the calcination time of Ag_XO@SBA-15.

In fact, well-dispersed Ag_2O and nanosize Ag can be observed after desulfurization from the result of TEM (Le et al. 2012), which ruled out the possibility of the reduction and agglomeration of silver particles during desulfurization. In the meantime, the corresponding XRD patterns of Ag_XO@SBA-15 samples with different regeneration treatments show that no Ag diffraction peak was detected in the sample solvent wash and re-calcine, indicating that neither individual operation of solvent wash nor calcination contributes to the agglomeration of silver particles. It is likely that the decomposition and agglomeration of Ag^+ to Ag^0 may occur during the thermal regeneration step, only in the presence of the polar organic compounds remaining on the Ag_XO@SBA-15 after solvent washing, as silver/silver oxide attracts N-containing organic solvents easily, i.e., ammonia solutions or cupric ammine (Starovoytov et al. 2007; Guan 1994; Yoon et al. 2003), which further accelerates the reductive decomposition of silver species, and the Ag^0 is more likely to accumulate on the silica surface. For comparison, instead of organic solvents, the desulfurization capacity of the spent adsorbent regenerated by deionized water wash followed with oxidative air treatment was tested and the desulfurization capacity was only 0.83 mg-S/g, lower than that from acetonitrile. This is likely due to the fact that water can hardly remove the residues adsorbed on the spent Ag_XO@SBA-15. Therefore, the choice of regeneration solvent must be cautious and is under further investigation.

Figure 11 shows the schematic diagram of the deactivation mechanism of Ag_XO@SBA-15. In the process of RADS, the active high-valence AgO oxidized BT in the model fuel and as well the Ag_2O species also acted as the oxidation catalyst to transform BT into BTO_2 in air. As the transformed BTO_2 has a stronger affinity for Ag_XO@SBA-15 than BT, thus BTO_2 and a small amount of BT were adsorbed onto Ag_XO@SBA-15 through BTO_2–(Si–OH) or BT–Ag_2O interaction, etc. After desulfurization, the active high-valence AgO was consumed, and more Ag_2O and a

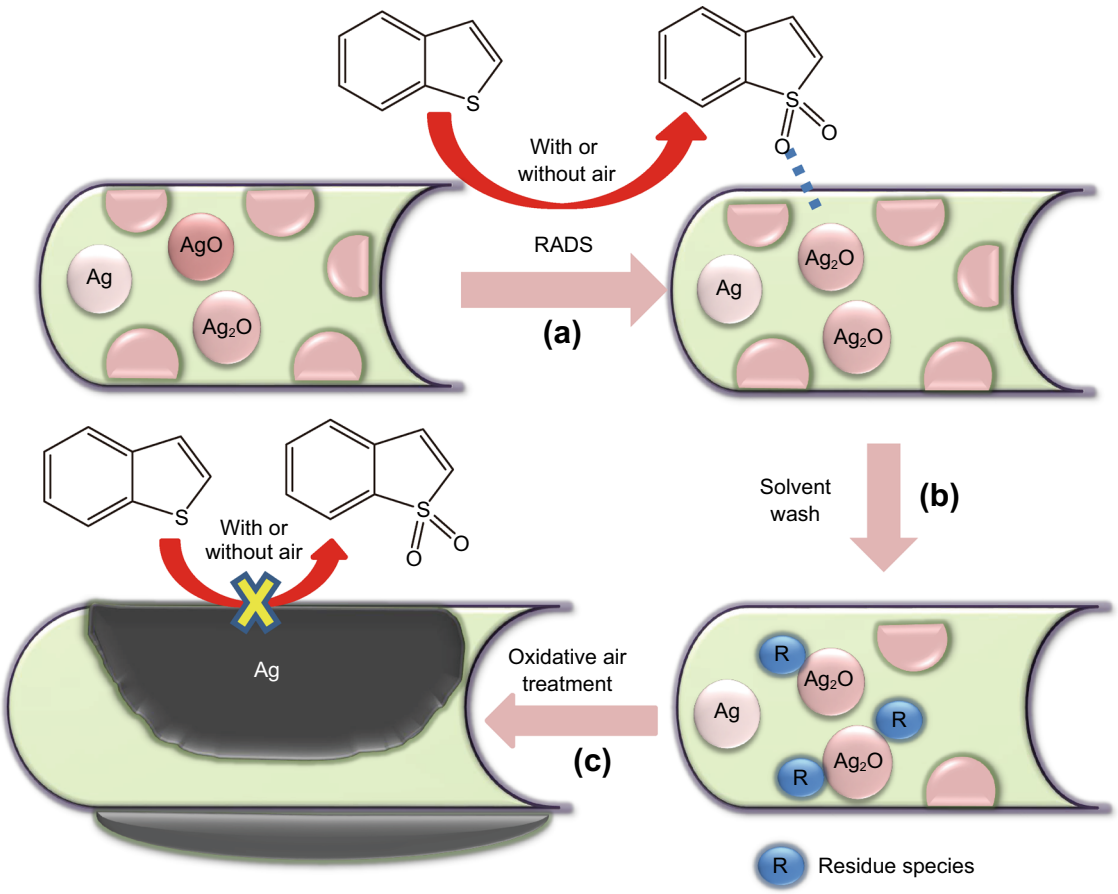

Fig. 11 Schematic diagram of the Ag_XO@SBA-15 deactivation in regeneration

small amount of Ag^0 were present well dispersed on the surface of the spent Ag_XO@SBA-15, as shown in Fig. 11a. In the first step of solvent washing in regeneration, BTO_2 and BT, some organic compounds (as shown as "residue" in Fig. 11) as well as alkanes, the alcohols by-products and the washing solvent itself (acetonitrile), etc., may be residual or adsorbed on the spent Ag_XO@SBA-15 after solvent washing (Fig. 11b), which also blocked the active sites on Ag_XO@SBA-15 for completely reversible RADS. As shown in Fig. 11c, with the surrounding organic species over Ag_XO@SBA-15, the decomposition of Ag_2O accelerates and the agglomeration of Ag^0 occurs during calcination up to 400 °C.

4 Conclusion

The regeneration of Ag_XO@SBA-15 for fuel desulfurization was investigated in this study. The recovery of desulfurization capacity using various solvents follows the order of acetonitrile > acetone > ethanol > methanol > water. It was noticeable that after the 1st-run regeneration, the desulfurization uptake of Ag_XO@SBA-15 decreased to 46% (1.56 mg-S/g), but the decrease is much milder in the latter regenerations. The deactivation mechanism in multiple cycles and during each regeneration step was further examined. XRD and TEM results suggested that high-valence AgO/Ag_2O in the fresh Ag_XO@SBA-15 altered to zero-valence Ag^0 after the 1st-run regeneration and aggregation of nanosize silver particles occurred, resulting in the complete loss of oxidizability of Ag species that oxidize BT to the corresponding sulfones with high adsorption affinity to the Ag_XO@SBA-15. Polar organic compounds strongly adsorbed (residual) on the spent Ag_XO@SBA-15 after solvent washing may contribute to the decomposition of Ag^+ to Ag^0 and silver aggregation during the second thermal regeneration step. Further mild aggregation of Ag^0 particles and gentle decrease in S_{BET} of Ag_XO@SBA-15 were noted in the regenerated Ag_XO@SBA-15 in the latter cycles, which likely contribute to the gradual decrease in adsorption capacity of BT. Cautious choice of regeneration conditions and strategies to rational design stabilized adsorbents may reduce the adsorbent deactivation.

Acknowledgements We gratefully acknowledge the research grants provided by the National Natural Science Foundation of China (21576093), Guangdong Natural Science Funds for Distinguished Young Scholars (2016A030306031), Guangdong Natural Science Foundation (2014A030312007) and Fundamental Research Funds for the Central Universities.

References

Agarwal P, Sharma DK. Comparative studies on the bio-desulfurization of crude oil with other desulfurization techniques and deep desulfurization through integrated processes. Energy Fuels. 2010;24(1):518–24. https://doi.org/10.1021/ef900876j.

Aronson BJ, Blanford CF, Stein A. Solution-phase grafting of titanium dioxide onto the pore surface of mesoporous silicates: synthesis and structural characterization. Chem Mater. 1997;9(12):2842–51. https://doi.org/10.1021/cm970180k.

Babich IV, Moulijn JA. Science and technology of novel processes for deep desulfurization of oil refinery streams: a review. Fuel. 2003;82(6):607–31. https://doi.org/10.1016/S0016-2361(02)00324-1.

Bhutto AW, Abro R, Gao S, Abbas T, Chen X, Yu G. Oxidative desulfurization of fuel oils using ionic liquids: a review. J Taiwan Inst Chem Eng. 2016;62:84–97. https://doi.org/10.1016/j.jtice.2016.01.014.

Borchert H, Shevchenko EV, Robert A, Mekis I, Kornowski A, Grübel G. Determination of nanocrystal sizes: a comparison of TEM, SAXS, and XRD studies of highly monodisperse $CoPt_3$ particles. Langmuir. 2005;21:1931–6. https://doi.org/10.1021/la0477183.

Butler OT, Cairns WRL, Cook JM, Davidson CM. 2014 atomic spectrometry update—a review of advances in environmental analysis. J Anal At Spectrom. 2015. https://doi.org/10.1039/c4ja90062f10.1039/c4ja90062f.

Chaiprapat S, Charnnok B, Kantachote D, Sung S. Bio-desulfurization of biogas using acidic biotrickling filter with dissolved oxygen in step feed recirculation. Bioresour Technol. 2015;179:429–35. https://doi.org/10.1016/j.biortech.2014.12.068.

Dai P, Yan TT, Yu XX, Bai ZM, Wu MZ. Two-solvent method synthesis of NiO/ZnO nanoparticles embedded in mesoporous SBA-15: photocatalytic properties study. Nanoscale Res Lett. 2016;11(1):226. https://doi.org/10.1186/s11671-016-1445-2.

Dou J, Zeng HC. Integrated networks of mesoporous silica nanowires and their bifunctional catalysis-sorption application for oxidative desulfurization. ACS Catal. 2014;4(2):566–76. https://doi.org/10.1021/cs400996j.

Fan Q, Zhao D, Dai Y. The research of ultra-deep desulfurization in diesel via ultrasonic irradiation under the catalytic system of H_2O_2–CH_3COOH–$FeSO_4$. Pet Sci Technol. 2009;27(3):302–14. https://doi.org/10.1080/10916460701707679.

George J, Shylesh S, Singh AP. Vanadium-containing ordered mesoporous silicas: synthesis, characterization and catalytic activity in the hydroxylation of biphenyl. Appl Catal A Gen. 2005;290:148–58. https://doi.org/10.1016/j.apcata.2005.05.012.

Gislason J. Phillips sulfur-removal process nears commercialization. Oil Gas J. 2001;99(47):72.

González J, Chen LF, Wang JA, Manríquez M, Limas R, Schachat P, et al. Surface chemistry and catalytic properties of VOX/Ti-MCM-41 catalysts for dibenzothiophene oxidation in a biphasic system. Appl Surf Sci. 2016;379:367–76. https://doi.org/10.1016/j.apsusc.2016.04.067.

Gu G, Xu J, Wu Y, Chen M, Wu L. Synthesis and antibacterial property of hollow SiO_2/Ag nanocomposite spheres. J Colloid Interface Sci. 2011;359(2):327–33. https://doi.org/10.1016/j.jcis.2011.04.002.

Guan Y. The dissolution behavior of silver in ammoniacal solutions with cupric ammine. J Electrochem Soc. 1994;141(1):91–6. https://doi.org/10.1149/1.2054715.

Guo J, Janik MJ, Song C. Density functional theory study on the role of ceria addition in $Ti_xCe_{1-x}O_2$ adsorbents for thiophene adsorption. J Phys Chem C. 2012;116(5):3457–66. https://doi.org/10.1021/jp2063996.

Ebin B, Yazici E, Gurmen S, Ozkal B. Preparation and characterization of nanocrystalline silver particles. TMS Annual Meeting. 2010:571–576.

Hobson JP. Physical adsorption. Crit Rev Solid State Mater Sci. 1973;4(1–4):221–45.

Juliao D, Gomes AC, Pillinger M, Valenca R, Ribeiro JC, Goncalves IS, et al. Desulfurization of liquid fuels by extraction and sulfoxidation using H_2O_2 and $[CpMo(CO)_3R]$ as catalysts. Appl Catal B Environ. 2018;230:177–83. https://doi.org/10.1016/j.apcatb.2018.02.036.

Kruk M, Jaroniec M. Application of large pore MCM-41 molecular sieves to improve pore size analysis using nitrogen adsorption measurements. Langmuir. 1997;13(23):6267–73. https://doi.org/10.1021/la970776m.

Kruk M, Jaroniec M. Gas adsorption characterization of ordered organic-inorganic nanocomposite materials. Chem Mater. 2001;13(10):3169–83. https://doi.org/10.1021/cm0101069.

Le Y, Mehmood F, Lee S, Greele J, Lee B, Seifert S, et al. Increased silver activity for direct propylene epoxidation via subnanometer size effects. Science. 2012;328(5975):224–8. https://doi.org/10.1126/science.1185200.

Lee KX, Valla JA. Investigation of metal-exchanged mesoporous Y zeolites for the adsorptive desulfurization of liquid fuels. Appl Catal B. 2017;201:359–69. https://doi.org/10.1016/j.apcatb.2016.08.018.

Lei W, Wenya W, Mominou N, Liu L, Li S. Ultra-deep desulfurization of gasoline through aqueous phase in situ hydrogenation and photocatalytic oxidation. Appl Catal B. 2016;193:180–8. https://doi.org/10.1016/j.apcatb.2016.04.032.

Li JR, Kuppler RJ, Zhou HC. Selective gas adsorption and separation in metal-organic frameworks. Chem Soc Rev. 2009;38(5):1477–504. https://doi.org/10.1039/b802426j.

Li LD, Xu CZ, Zheng MQ, Chen XH. Effect of B_2O_3 modified Ag/TiO_2–Al_2O_3 adsorbents on the adsorption desulfurization of diesel. J Fuel Chem Technol. 2015;43(8):990–7. https://doi.org/10.1016/S1872-5813(15)30028-1.

Li M, Zhou Z, Zhang F, Chai W, Zhang L, Ren Z. Deep oxidative-extractive desulfurization of fuels using benzyl-based ionic liquid. AIChE J. 2016a;62(11):4023–34. https://doi.org/10.1002/aic.15326.

Li S-W, Gao R-M, Zhang R-L, Zhao JS. Template method for a hybrid catalyst material POM@MOF-199 anchored on MCM-41: highly oxidative desulfurization of DBT under molecular oxygen. Fuel. 2016b;184:18–27. https://doi.org/10.1016/j.fuel.2016.06.132.

Lu Z, Streets DG, Zhang Q, Wang S, Carmichael GR, Cheng YF, et al. Sulfur dioxide emissions in China and sulfur trends in East

Asia since 2000. Atmos Chem Phys. 2010;10(13):6311–31. https://doi.org/10.5194/acp-10-6311-2010.

Lu Z, Guo E, Zhong H, Tian Y, Yao Y, Lu S. Kinetic modeling of the extraction-oxidation coupling process for the removal of dibenzothiophene. Energy Fuels. 2016;30(9):7214–20. https://doi.org/10.1021/acs.energyfuels.6b01552.

Ma X, Zhou A, Song C. A novel method for oxidative desulfurization of liquid hydrocarbon fuels based on catalytic oxidation using molecular oxygen coupled with selective adsorption. Catal Today. 2007;123(1–4):276–84. https://doi.org/10.1016/j.cattod.2007.02.036.

Malakooti R, Parsaee Z, Hosseinabadi R, Oskooie HA, Heravi MM, Saeedi M, et al. $[Cu(bpdo)_2{\cdot}2H_2O]^{2+}$-supported SBA-15 nanocatalyst for efficient one-pot synthesis of benzoxanthenone and benzochromene derivatives. C R Chim. 2013;16(9):799–806. https://doi.org/10.1016/j.crci.2013.03.007.

Miao G, Ye F, Wu L, Ren X, Xiao J, Li Z, et al. Selective adsorption of thiophenic compounds from fuel over TiO_2/SiO_2 under UV-irradiation. J Hazard Mater. 2015;300:426–32. https://doi.org/10.1016/j.jhazmat.2015.07.027.

Miao G, Huang D, Ren X, Li X, Li Z, Xiao J. Visible-light induced photocatalytic oxidative desulfurization using $BiVO_4/C_3N_4$@-SiO_2 with air/cumene hydroperoxide under ambient conditions. Appl Catal B. 2016;192:72–9. https://doi.org/10.1016/j.apcatb.2016.03.033.

Mohammadian M, Ahmadi M, Khosravinikou MR. Adsorptive desulfurization and denitrogenation of model fuel by mesoporous adsorbents (MSU-S and CoO-MSU-S). Pet Sci Technol. 2017;35(6):608–14.

Ocakoglu K, Mansour ShA, Yildirimcan S, Al-Ghamdi AA, El-Tantawy F, Yakuphanoglu F. Microwave-assisted hydrothermal synthesis and characterization of ZnO nanorods. Spectrochim Acta Part A Mol Biomol Spectrosc. 2015;148:362–8. https://doi.org/10.1016/j.saa.2015.03.106.

Perkas N, Lipovsky A, Amirian G, Nitzan Y, Gedanken A. Biocidal properties of TiO_2 powder modified with Ag nanoparticles. J Mater Chem B. 2013;1(39):5309. https://doi.org/10.1039/c2tb00337f.

Piccinino D, Abdalghani I, Botta G, Crucianelli M, Passacantando M, Di Vacri ML, et al. Preparation of wrapped carbon nanotubes poly(4-vinylpyridine)/MTO based heterogeneous catalysts for the oxidative desulfurization (ODS) of model and synthetic diesel fuel. Appl Catal B. 2017;200:392–401. https://doi.org/10.1016/j.apcatb.2016.07.037.

Qin J-X, Tan P, Jiang Y, Liu X-Q, He Q-X, Sun L-B. Functionalization of metal–organic frameworks with cuprous sites using vapor-induced selective reduction: efficient adsorbents for deep desulfurization. Green Chem. 2016;18(11):3210–5. https://doi.org/10.1039/c6gc00613b.

Qiu L, Zou K, Xu G. Investigation on the sulfur state and phase transformation of spent and regenerated S zorb sorbents using XPS and XRD. Appl Surf Sci. 2013;266:230–4. https://doi.org/10.1016/j.apsusc.2012.11.156.

Ren X, Miao G, Xiao Z, Ye F, Li Z, Wang H, et al. Catalytic adsorptive desulfurization of model diesel fuel using TiO_2/SBA-15 under mild conditions. Fuel. 2016;174:118–25. https://doi.org/10.1016/j.fuel.2016.01.093.

Sévignon M, Macaud M, Favre-Réguillon A, Schulz J, Rocault M, Faure R, et al. Ultra-deep desulfurization of transportation fuels via charge-transfer complexes under ambient conditions. Green Chem. 2005;7(6):413. https://doi.org/10.1039/b502672e.

Sing KSWE, Everett DH, Haul RAW, Moscou L, Pierotti RA, Rouquerol J, Siemieniewska T. Reporting physisorption data for gas/solid systems with special reference to the determination of surface area and porosity. Pure Appl Chem. 1985;57(11):603–19.

Song C. An overview of new approaches to deep desulfurization for ultra-clean gasoline, diesel fuel and jet fuel. Catal Today. 2003;86(1–4):211–63. https://doi.org/10.1016/s0920-5861(03)00412-7.

Song C, Ma X. New design approaches to ultra-clean diesel fuels by deep desulfurization and deep dearomatization. Appl Catal B. 2003;41(1–2):207–38. https://doi.org/10.1016/s0926-3373(02)00212-6.

Starovoytov ON, Kim NS, Han KN. Dissolution behavior of silver in ammoniacal solutions using bromine, iodine and hydrogen-peroxide as oxidants. Hydrometallurgy. 2007;86(1–2):114–9. https://doi.org/10.1016/j.hydromet.2006.11.009.

Verma P, Kuwahara Y, Mori K, Yamashita H. Synthesis and characterization of a Pd/Ag bimetallic nanocatalyst on SBA-15 mesoporous silica as a plasmonic catalyst. J Mater Chem A. 2015;3(37):18889–97. https://doi.org/10.1039/c5ta04818d.

Wu P, Zhu W, Dai B, Chao Y, Li C, Li H, et al. Copper nanoparticles advance electron mobility of graphene-like boron nitride for enhanced aerobic oxidative desulfurization. Chem Eng J. 2016;301:123–31. https://doi.org/10.1016/j.cej.2016.04.103.

Xia D. The oxidation-extraction desulfurization of FCC gasoline. Pet Sci Technol. 2008;26(16):1887–92. https://doi.org/10.1080/10916460701426072.

Xiao J, Li Z, Liu B, Xia Q, Yu M. Adsorption of benzothiophene and dibenzothiophene on ion-impregnated activated carbons and ion-exchanged Y zeolites. Energy Fuels. 2008;22(6):3858–63. https://doi.org/10.1021/ef800437e.

Xiao J, Bian G, Zhang W, Li Z. Adsorption of dibenzothiophene on Ag/Cu/Fe-supported activated carbons. J Chem Eng Data. 2010;55(12):5818–23. https://doi.org/10.1021/je1007795.

Xiao J, Sitamraju S, Chen Y, Janik M, Song C. Air-promoted adsorptive desulfurization over $Ti_{0.9}Ce_{0.1}O_2$ mixed oxides from diesel fuel under ambient conditions. ChemCatChem. 2013;5(12):3582–6. https://doi.org/10.1002/cctc.201300329.

Xiao J, Wu L, Wu Y, Liu B, Dai L, Li Z, et al. Effect of gasoline composition on oxidative desulfurization using a phosphotungstic acid/activated carbon catalyst with hydrogen peroxide. Appl Energy. 2014;113:78–85. https://doi.org/10.1016/j.apenergy.2013.06.047.

Xiao J, Sitamraju S, Chen Y, Watanabe S, Fujii M, Janik M, et al. Air-promoted adsorptive desulfurization of diesel fuel over Ti-Ce mixed metal oxides. AIChE J. 2015;61(2):631–9. https://doi.org/10.1002/aic.14647.

Ye FMG, Wu Y, Li Z, Song CS, Xiao J. [O]-induced reactive adsorptive desulfurization of fuel over Ag_XO@SBA-15 under ambient conditions. Chem Eng Sci. 2017. https://doi.org/10.1016/j.ces.2017.04.032.

Yoon H, Sohn JS, Kim NS, Han KN. Dissolution behavior of silver/silver oxides in ammoniacal solutions. Miner Metall Process. 2003;20(1):31–5.

Zhang X, Dong H, Zhao D, Wang Y, Wang Y, Cui L. Effect of support calcination temperature on Ag structure and catalytic activity for CO oxidation. Chem Res Chin Univ. 2016a;32(3):455–60. https://doi.org/10.1007/s40242-016-5377-2.

Zhang Y, Yuan S, Feng X, Li H, Zhou J, Wang B. Preparation of nanofibrous metal-organic framework filters for efficient air pollution control. J Am Chem Soc. 2016b;138(18):5785–8. https://doi.org/10.1021/jacs.6b02553.

Zvereva VV, Trunova VA. Determination of the elemental composition of tissues of the cardiovascular system by atomic spectrometry, mass spectrometry and X-ray spectrometry methods. J Anal Chem. 2012;67(7):613–31. https://doi.org/10.1134/s1061934812070064.